

## Article

# Numerical Calculation of the Arc-Sprayed Particles' Temperature in Transient Thermal Field

Stefan Lucian Toma <sup>1,\*</sup> , Daniela-Lucia Chicet <sup>2,\*</sup> and Alin-Marian Cazac <sup>1,\*</sup>

<sup>1</sup> Department of Materials Engineering and Industrial Safety, Faculty of Materials Science and Engineering, Gheorghe Asachi Technical University of Iasi, 700050 Iasi, Romania

<sup>2</sup> Materials Science Department, Materials Science and Engineering Faculty, Gheorghe Asachi Technical University of Iasi, 700050 Iasi, Romania

\* Correspondence: stefan-lucian.toma@academic.tuiasi.ro (S.L.T.); daniela-lucia.chicet@academic.tuiasi.ro (D.-L.C.); alin-marian.cazac@academic.tuiasi.ro (A.-M.C.)

**Abstract:** The physical and mechanical properties of the coatings produced by electric arc thermal spraying are closely related to the velocity and temperature of the particles that interact with the substrate surface. Knowing the temperature variation of the sprayed particles allows establishing their aggregation state, respectively determining the spraying distance, so that the state of aggregation of the particles at the impact moment is predominantly liquid. Obviously, when the sprayed particle passes through the spray cone, it cools continuously due to the low and variable temperature of the entrainment gas. This paper aims to determine analytically the thermal behavior of the particles entrained by the gas jet formed at the thermal spraying in an electric arc, depending on the variable temperature, existing along the spraying cone. In this sense, by modeling with finite elements, using the ANSYS program, the temperature inside the spray jet was determined, and by a mathematical model carried out based on the thermal balance equations, the thermal profile of the sprayed particles was determined. The thermal profile demonstrates that their temperature suddenly increases to the solidification temperature, then increases to the melting temperature—due to the latent heat of solidification, after which it decreases to 300 K.

**Keywords:** arc spray process; particles; thermal profile



**Citation:** Toma, S.L.; Chicet, D.-L.; Cazac, A.-M. Numerical Calculation of the Arc-Sprayed Particles' Temperature in Transient Thermal Field. *Coatings* **2022**, *12*, 877. <https://doi.org/10.3390/coatings12070877>

Academic Editor: Christian Mitterer

Received: 6 May 2022

Accepted: 18 June 2022

Published: 21 June 2022

**Publisher's Note:** MDPI stays neutral with regard to jurisdictional claims in published maps and institutional affiliations.



**Copyright:** © 2022 by the authors. Licensee MDPI, Basel, Switzerland. This article is an open access article distributed under the terms and conditions of the Creative Commons Attribution (CC BY) license (<https://creativecommons.org/licenses/by/4.0/>).

## 1. Introduction

One of the most cost-effective methods of coating surfaces by thermal spraying is that of electric arc spraying, because the costs of purchasing and operating such equipment can be quickly amortized, due to the high productivity and versatility of the materials that can be thus sprayed [1–3]. The electric arc deposition process is based on the formation of an electric arc between the two consumable wires directed through the pistol head, on the atomization of the molten material by means of a carrier gas pressured jet and the acceleration of the particles thus produced towards the substrate surface [4–6]. Upon impact with the substrate, the particles flatten and deposit in the form of splats, thus giving rise to a coating composed of successive layers [7–10]. The steps of this mechanism are shown schematically in Figure 1 [11].

In contrast to the efficiency of this deposition process, there are a number of disadvantages, among which the following can be mentioned: smoke release during deposition, higher porosity of the coating compared to other thermal spraying methods, and an increased percentage of oxides in the coating caused by oxidation of the droplets in contact with the working atmosphere [12–14].

A multitude of studies are available in the literature, in which attempts are made to experimentally solve these drawbacks by varying the working parameters, an example being the study [15], in which it was analyzed how the type of carrier gas (Ar, N, O, air) influences the oxidation degree of the arc coatings. Other studied parameters were the wire

feed rate [16] and its influence on the adhesion to the substrate, the oxidation resistance of the arc-sprayed coatings [17], or the influence of the substrate texture on the coating quality [18]. Furthermore, the phenomena in the spray jet were analyzed using high-speed recording cameras [19], and the thermal diffusivity  $\alpha$  of the coatings was measured by thermal wave interferometry [20].

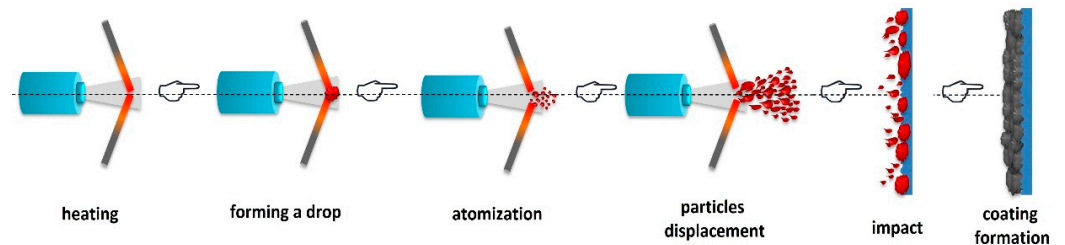


**Figure 1.** Coating formation mechanism by electric arc thermal spraying [11].

From the studies on the influence of working parameters on the quality of arc spray coatings, it appears that the success of a quality coating is closely related to the temperature at which the particles reach the substrate. It has been found that a too-low temperature causes the material to go into a semi-molten, viscous state, which leads to the formation of less adherent splats, so that there is a risk of producing a coating with low cohesion in the layer, caused mainly by the increase of gaps between the splats [21].

With the evolution of finite-element analysis and numerical simulation software for heat transfer phenomena, a general trend of the extension of the research approach from case studies to numerical analysis and simulation can be observed [22–24]. Thus, the analysis of particular phenomena leads to the establishment of models on the basis of which the simulation of the influence of the thermal spraying process phenomena can be carried out, in order to achieve efficiency in terms of cost versus optimization time. R. Tamaki et al. carried out a series of studies both practically [25] and by Computational Fluid Dynamics (CFD) analysis [26,27] on how the modification of the spray jet configuration, using a plate mounted between the two wires upstream of the arc point, influenced the flow field and the pulverization of the droplets. It was observed that the mass of the molten wire changes once with the mounting position of the plate, and the larger the expansion waves on the plate sides, the smaller the mass of the molten wire is. Another study aiming at the optimization by geometry modification is [28], in which a model of an arc spray gun was realized with CFD, and the gas flow inside and outside the spray gun was analyzed. It was observed that moving the intersection point from the nozzle outside to the nozzle exit and a moderate intersection angle are beneficial for the flow velocity distribution and droplet atomization.

The influence of spray nozzle geometry and numerical prediction of the splat diameter distribution was studied by CFD analysis in [29], with three different models being considered: closed nozzle with green cap and converging orifice (C/CL), closed nozzle with a converging-diverging orifice (CD/CL), and open nozzle with a converging-diverging orifice (CD/OP). It was observed that the third variant, with open nozzle, is the least efficient due to the large distance between the intersection point of the wires and the nozzle outlet, while the second variant provides a smaller average diameter and a better splat distribution.

In study [30], the arc spray process was analyzed by a three-dimensional model, using the Fluent CFD code to study the jet inside and outside the spray head, and two different  $k-\epsilon$  type turbulence models suitable for the study of round jets were tested. A completely different behavior from that of such a jet (round) was observed due to the complexity of the component elements, significantly divergent in the horizontal and vertical planes. Another use of the numerical model is the one from the study [31], based on the capability to handle free surface evolution during droplet flattening, fluid flow, heat transfer, and solidification phase change in the molten droplet, being reported the dynamics of air entrapment and the formation of pores in thermal spraying coating by considering the realistic conditions.

It was also studied how numerical modeling can provide solutions to improve the mechanical characteristics of arc-sprayed coatings, an example being given in study [32], in which coatings made of 625 alloy were subjected to multiple experimental tests and analytical and numerical simulations, to determine the elastic modulus of the coating. Another example is the one from the study [33], where a mathematical model was developed to calculate the residual stresses of arc-produced coatings, considering the quenching stress generated during the coating deposition process and the thermal stress generated during the cooling process and establishing a corresponding relationship among the number of coating layers, the temperature gradient, and the residual stress.

As can be seen, there is no modeling of particle behavior on the route from the atomization nozzle to the substrate, in the literature. Several studies on the numerical analysis of the plasma spray process have been carried out, regarding the analysis of the arc dynamics and its effect on the distributions of the temperature and flow field both inside and outside of the torch [34], the deep neural networks that have an excellent ability to express the governing equations of thermal plasmas [35], the deposition behavior and oxidation mechanism of the coatings [36], or a proposed computational approach that can predict the mechanical properties [37]. The results of a numerical simulation based on a 3D (Ansys Fluent 19.0) model and experimental measurements were compared and thus validated the flow-velocity field directly and the distribution of particle mass concentration indirectly in the case of internal rotating plasma spraying (IRPS) coatings [38].

The hydrodynamic and electromagnetic phenomena occurring in the plasma spray gun in the case of coating with a TriplexPro™-200 three-cathode device were simulated using a three-dimensional numerical model, but without taking into account the marginal areas of the electrode surfaces. In the same study [39], another model was performed in order to approximate the plasma parameters in the free jet. Both models were validated using a complex analysis system based on argon emission computed tomography by analyzing the temperature distribution recorded during the experiment. The results obtained were used to evaluate the influence of process parameters on the plasma jet characteristics and to understand the physical phenomena occurring inside the spray gun.

In [40], further numerical models were presented, developed with the commercial Fluent 6.3 software, in order to analyze how the arc fluctuations developed inside the spray gun influence the formation of the plasma jet, i.e., its temperature and velocity. The plasma jet coating technology was also analyzed in [41], in which a three-dimensional numerical model was developed, one of the variables being time. This model was extended to include areas inside, as well as outside the spray torch, and the analysis of the plasma spray jet was realized based on the data provided via the Enthalpy probe system. The most important conclusion drawn from this study is that the temperature and velocity distribution inside the plasma jet exhibits a significant three-dimensional asymmetric distribution.

Another comparative study developed using numerical simulations is [42], in which the spraying mode of a YSZ-type powder at the same voltage (electrical input power) was analyzed using plasma jet spray guns with one cathode, respectively three cathodes. It was observed that the jet obtained with the three-cathode gun has a higher velocity and temperature than that generated with the one-cathode gun. Thus, it could be concluded that in the case of the three-cathode gun, a much more uniform distribution of the particles introduced in the spray jet can be obtained in the area of higher velocity and temperature regardless of their size, if an area with lower temperature is chosen as the powder injection point.

It follows from the above that it is justified to carry out studies regarding the jet temperature variation in the process of thermal arc spraying, because it plays an important role in the thermal behavior of the particles in the gas jet. Knowing how the temperature within the carrier gas varies allows the determination of the particle temperature at any point within the spray jet, i.e., how the temperature of the sprayed particle varies.

The objective of the present study is to investigate the effect of the temperature of the entrainment gas jet on the temperature of the sprayed particles, using a CFD model (for the determination of the spray jet temperature) and a mathematical model built on the

basis of the thermal equilibrium equation (used to approximate the thermal behavior of the sprayed particles).

## 2. Computational Setup

### 2.1. The Modeling of the Arc Spraying Process

The temperature of the spray jet, in the process of electric arc thermal spraying, has an important role on the thermal behavior of the particles in the gas jet. Knowing the temperature variation mode inside the entrainment gas jet allows the determination of the particle temperature at any point within the spray domain, respectively the variation mode of the sprayed particle temperature.

In order to determine the temperature variation inside the entrainment gas jet, we used the Ansys—Computational Fluid Dynamic program (Ansys CFD), which consists of a solver specialized in thermal transfer phenomena [43,44]. The geometric model was realized with the help of the drawing module of the ANSYS program and was assimilated with a cylindrical tube with thin walls and with the lateral surface adiabatically isolated from the outside environment, resembling the one used in a previous study [21]. This model has one closed end and is provided with a 3 mm-diameter pipe through which the compressed air enters with a pressure of 5 bar and a temperature  $T_{\text{air}} = 298 \text{ K}$  (a value specific to the working conditions when spraying in an electric arc). The schematic representation of the model is presented in Figure 2, and its dimensions are resumed in Table 1.

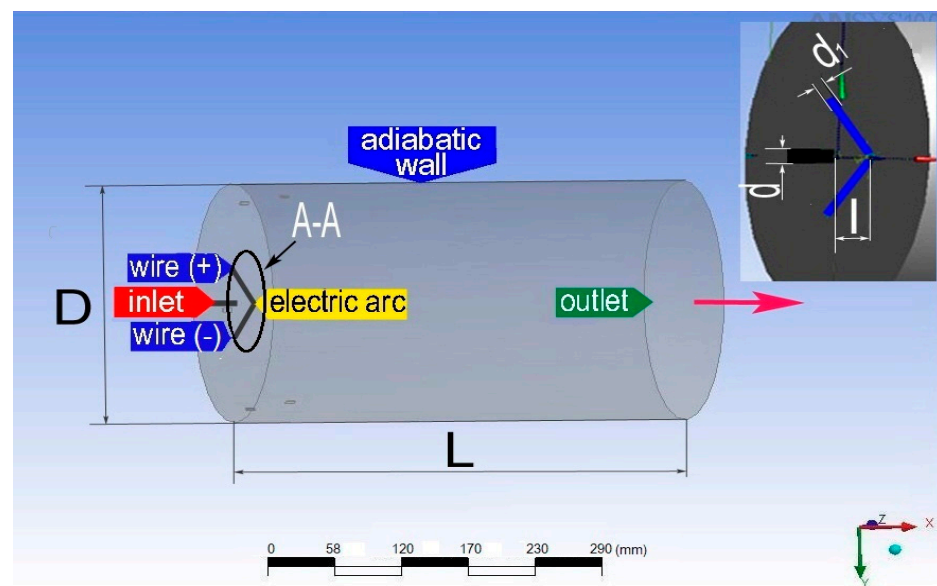


Figure 2. Schematic representation and loading sketch of the three-dimensional model [21].

Table 1. The geometrical dimensions of the model.

Dimensions	Symbol	Value
Total length of the cylinder	L	400 mm
Cylinder diameter—at the outlet	D	240 mm
Compressed air pipe diameter—at the inlet	d	3 mm
Wire diameter	$d_1$	0.8 mm
Wire tilt angle		$30^\circ$
Distance nozzle—arc	l	20 mm

Inside the model, at the output of the nozzle, the jet of the compressed air passes over the superheated surface of the electric arc ( $T_{\text{arc}} = 4500 \text{ K}$ ), which is formed at the contact of the two wires, tilted from the cylinder axis at an angle of  $30^\circ$ . The thermal transfer, from this

level, is carried out by forced convection, and the thermal transfer model, chosen through the software, was that of thermal energy. The fluid flow regime is subsonic ( $M < 1$ , where  $M$  is the Mach number), and the gas jet temperature inside the model varies continuously, so that the considered thermal regime is transient. The schematic representation of the loaded model is presented in Figure 2, and the values of the initial state parameters are presented in Table 2. The geometric dimensions of the model allow the consideration of the outer surface as an adiabatic surface.

**Table 2.** Initial parameters.

Parameters	Symbol	Value
Compressed air pressure—at the inlet	$P_{\text{inlet}}$	5 bar
Compressed air velocity—at the outlet	$v_{\text{outlet}}$	0.0173 m/s
Compressed air temperature	$T_{\text{air}}$	298 K
Local temperature of the electric arc	$T_{\text{arc}}$	4500 K
Wire tilt angle		30°
Nozzle—arc distance	$l$	20 mm
Average wire temperature between “arc point” and wire entry point in the model	$T_{\text{wire}}$	800 K
The degree of turbulence of the compressed air at the inlet		5%
Flow regime		subsonic
Exterior wall surface type		polished, adiabatic
The position of the outer wall		fixed

The values of the initial parameters (compressed air pressure, nozzle–arc distance, compressed air temperature), presented in Table 2, are similar to the parameters used by Toma et al. [11], in a study in which qualitative deposits were obtained. The degree of turbulence adopted was minimal, its value being chosen from those available through the software. The compressed air outlet speed was calculated by the software based on the continuity equation and the geometric dimensions of the model.

The values of  $T_{\text{arc}}$  and  $T_{\text{wire}}$  are average values, determined by us under laboratory conditions, on aluminum wires with diameters of 1.6 mm and applying arc voltages of 28 V.

The temperature of the compressed air jet was determined using: the continuity Equation (1), the moment Equation (2), and the energy Equation (3) [45].

$$\frac{\partial(\rho \cdot v_x)}{\partial x} + \frac{\partial(\rho \cdot v_y)}{\partial y} + \frac{\partial(\rho \cdot v_z)}{\partial z} + \frac{\partial \rho}{\partial t} = 0, \quad (1)$$

$$\frac{\partial \rho_f v_f}{\partial t} + \nabla \cdot (\rho_f \cdot v_f \otimes v_f) = \nabla \cdot (p \cdot \delta + \eta_f (\nabla v_f + (\nabla v_f)^T)) + S_M, \quad (2)$$

$$\frac{\partial \rho_f h_{tot}}{\partial t} - \frac{\partial p}{\partial t} + \nabla \cdot (\rho_f v_f h_{tot}) = \nabla \cdot (\lambda \nabla T) + S_E, \quad (3)$$

where  $h_{tot} = h + \frac{1}{2}v_f^2$

For the turbulence model, the  $k-\varepsilon$  criterion was adopted, and the control setup of the solver was realized by:

- Advection scheme: high resolution;
- Flow duration: 0.5 s;
- Maximum number of iterations: 40;
- Maximum root-mean-squared (RMS) convergence criterion:  $10^{-4}$ .

In order to evaluate the results of the analysis, we used:

- Two perpendicular axial planes (xOy and xOz), as presented in Figure 3a;
- A family of 20 transverse planes arranged at a distance  $g = 20$  mm from each other, as presented in Figure 3a;

- A system of 5 directions (numbered from 1 to 5), inclined with an angle of  $2.14^\circ$  relative to each other, as presented in Figure 3b;
- A system of 20 transverse directions located in the transverse planes, spaced apart at  $f = 20$  mm, as presented in Figure 3b.

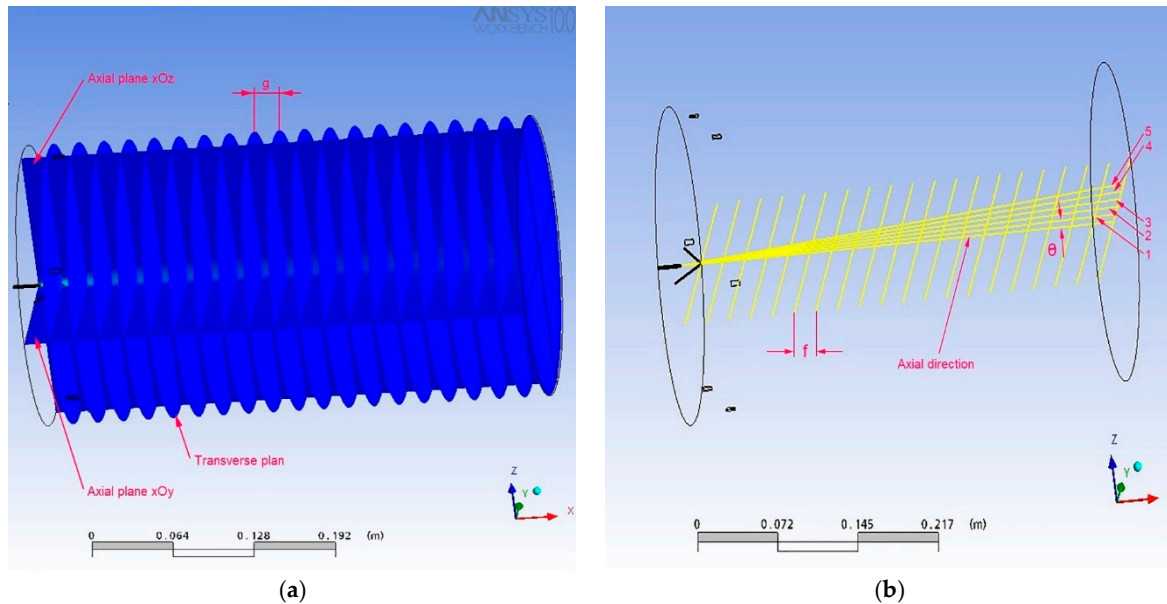


Figure 3. (a) Analysis plans; (b) directions of analysis.

## 2.2. The Mathematical Model

In order to determine the temperature of a spherical particle in the spraying jet, at a certain moment “ $t$ ”, we considered the following simplifying hypotheses:

- The shape of the particle is spherical, with a  $d_p$  diameter, placed at a distance of 20 mm from the “arc point”;
- The particle moves through the fluid with a velocity  $v_{pi} = 60$  m/s, [46];
- The fluid moves at a constant speed  $v_{fi} = 250$  m/s (in accordance with the results obtained by Vardelle, M. et al. [47]);
- $T_{fi}$  values are variable and were obtained by numerical simulation;
- At the initial moment  $t_0 = 0$ , the particles are in the liquid state, at the  $T_1$  temperature;
- The amount of heat transferred by radiation is negligible.

In these conditions, the general equation of thermal balance that characterizes the cooling process of the particle, with the temperature  $\partial T$ , in the time frame  $\partial t$  in which the solidification of a liquid fraction is also produced,  $V_p \cdot \partial f_s$ , is:

$$-\alpha_f \cdot A_p \cdot (T_p - T_f) + \lambda_p \cdot \rho_p \cdot V_p \cdot \frac{\partial f_s}{\partial t} = \rho_p \cdot V_p \cdot C_{pp} \cdot \frac{\partial T}{\partial t}, \quad (4)$$

The first term placed on the left side of the equal sign in Equation (4) represents the amount of heat transferred by convection to the entrainment gas, while the second term represents the amount of heat released by the solidification of a fraction ( $\partial f_s$ ) of the liquid volume  $V_p$ . The factor  $\frac{\partial T}{\partial t}$  represents the cooling velocity, and the factor  $\frac{\partial f_s}{\partial t}$  represents the solidification velocity of the particle.

The convection heat exchange coefficient  $\alpha_f$  was determined using the Rantze and Marshal Equation (5) [48,49] and the dimensionless Prandtl (6) and Reynolds (7) numbers.

$$\alpha_f = \frac{k_g}{d_p} \left( 2 + 0.6 \sqrt{Re} \cdot \sqrt[3]{Pr} \right), \quad (5)$$

$$Pr = \frac{C_{pf} \cdot \nu}{|v_p - v_g|}, \quad (6)$$

$$Re = \frac{\rho_f \cdot d_p \cdot |v_p - v_f|}{\eta} = \frac{d_p \cdot |v_p - v_f|}{\nu}, \quad (7)$$

where  $v_p - v_f$ —is the relative velocity between the particle and the fluid (m/s).

The latent solidification heat ( $\lambda_p$ ) released by the solidified volume ( $f_s \cdot V_p$ ) was calculated using Equation (8).

$$\lambda_p = \lambda_u - (C_l - C_s) \cdot (T_L - T_s), \quad (8)$$

The specific heat of the particle ( $C_{pp}$ ) was calculated with the help of Equation (9):

$$C_{pp} = C_l - (C_l - C_s) \cdot f_s, \quad (9)$$

Equation (4) describes the thermal behavior of the molten and sprayed particle, being applicable along the entire length of the spray jet. The term  $\lambda_p \cdot \frac{\partial f_s}{\partial t}$  is neglected in the particle atomization phase. Furthermore, the thermal state of the particle in the atomization phase is given by the value of the specific heat of the liquid phase. The phase changes, accompanied by solidification, are observed during spraying, as well as during the impact of the particle with the substrate surface.

In the hypothesis that the internal solidification of the undercooled particle occurs on the basis of a diffusion-free mechanism and the liquid–solid separation interface (L/S) is flat, then the advance velocity of the solidification interface can be written as directly proportional to the difference between the temperature corresponding to the liquid curve (specific for the considered alloy) and particle temperature [50], according to Equation (10).

$$\frac{dx}{dt} = k_i \cdot (T_L - T_p), \quad (10)$$

In this Equation (10), the factor  $k_i$  represents the advance coefficient of the solidification front relative to the degree of undercooling of the melt. The value of  $k_i$  is determined experimentally. For electric arc spraying, the value  $k_i = 0.02 \text{ ms}^{-1} \text{ T}^{-1}$  was considered, also valid in the case of metal melt atomization processes, realized in order to obtain small-sized powders [51].

Considering that the solidification phenomenon is developing at the particle surface, the fraction of liquid solidified during undercooling ( $df_s$ ) at the advance of the solidification front over a very short distance  $dx$  is given by Equation (11) [52]:

$$\frac{df_s}{dx} = \frac{1}{d_p} \cdot \left[ 3 \cdot \left( \frac{x}{d_p} \right) - \frac{3}{2} \cdot \left( \frac{x}{d_p} \right)^2 \right], \quad (11)$$

Substituting in Equation (4) the calculation formulas for area and volume, Equations (10) and (11), and simplification with the factor ( $\rho_p \cdot V_p \cdot C_{pp}$ ), this results in Equation (12).

$$\frac{\lambda_p}{C_{pp}} \left\{ \frac{1}{d_p} \left[ 3 \cdot \left( \frac{x}{d_p} \right) - \frac{3}{2} \left( \frac{x}{d_p} \right)^2 \right] \right\} \frac{dx}{dt} + \frac{6 \cdot \alpha_f}{\rho_p \cdot d \cdot C_{pp}} \left[ \frac{1}{k_i} \frac{dx}{d\tau} + (T_f - T_L) \right] = \frac{\partial T_p}{\partial t}; \quad (12)$$

By deriving Equation (10) in relation to the time, the following Equation (13) was obtained:

$$\frac{d^2x}{dt^2} = -k_i \cdot \frac{dT_p}{dt}; \quad (13)$$

By substituting Equation (13) in Equation (12) and by rearranging the terms, Equation (14) results.

$$\frac{d^2x}{dt^2} = (D_1 \cdot x^2 + D_2 \cdot x + D_3) \frac{dx}{dt} + D_4; \quad (14)$$

where:

$$\begin{aligned} D_1 &= \frac{3}{2} \cdot \frac{k_1 \cdot \lambda_p}{C_{pp} \cdot d^3}, \\ D_2 &= \frac{-3k_1 \lambda_p}{C_{pp} \cdot d_p^3}, \\ D_3 &= \frac{-6 \cdot \alpha_f}{C_{pp} \cdot d \cdot \rho_p}, \\ D_4 &= \frac{-6 \alpha_f \cdot k_i (T_f - T_L)}{\rho_p \cdot d_p \cdot C_{pp}}. \end{aligned}$$

By integrating Equation (14) in relation to time, the advance velocity of the solidification interface is obtained (15), in the case of a particle of a certain material, when the temperature decreases with the value  $|T_f - T_L|$ :

$$\frac{dx}{dt} = \frac{1}{3} D_1 \cdot x^3 + \frac{1}{2} D_2 \cdot x^2 + D_3 \cdot x + D_4 \cdot t + D_5 \quad (15)$$

The term  $D_5$  from Equation (15) is obtained from the limit condition, assuming that the solidification phenomenon takes place in those points on the particle's surface at which the temperature  $T_p = T_s$ , corresponding to the initial moment ( $t = 0$ ), respectively  $x = 0$ , as calculated in Equation (16).

$$D_5 = k_i \cdot (T_l - T_s); \quad (16)$$

Equation (16) shows that the velocity of the advance of the solidification front inside a particle cooled by forced convection is dependent on the thermophysical constants of the material, on the particle diameter ( $d$ ), and on the difference between the gas fluid temperature ( $T_f$ ) and the liquid temperature ( $T_L$ ).

By a quick analysis of Equation (16), it is observed that:

- If  $T_f > T_L$ , the term  $D_4 < 0$  and the advance velocity of the solidification front inside the particle are very low;
- If  $T_f = T_L$ , we have  $D_4 = 0$ , and the solidification front does not advance inside the particle;
- If  $T_f < T_L$ , then  $D_4 > 0$  and the advance velocity of the solidification front inside the particle increases.

### 3. Experimental Setup

In order to validate the results obtained by analytical calculation, coatings of aluminum alloy 01S (manufactured by Tafa Praxair, Indianapolis, IN, USA) with the following chemical composition were experimentally deposited: 5.2 wt%Si, 0.8 wt% Fe, 2.6 wt%Cr, 0.8 wt% Ti, 0.05 wt% Mn, Al balance (wt%). The substrate used for deposition was in the form of metal strips, made from C15 steel (DIN 17210-1652), with the following chemical composition: 0.14 wt%C, 0.43 wt%Mn, 0.3 wt%Cr, 0.3 wt%Ni, 0.15 wt%Si, 0.04 wt%P, and 0.04 wt%S. The steel specimens were previously prepared by blasting at 6 bar pressure with corundum ( $Al_2O_3$ , 120  $\mu$ m grain size), chemical cleaning in an ultrasonic bath to remove mechanical impurities, and air-dried at 200 °C. For this experimental study, the substrate was positioned at different spraying distances (nozzle–substrate distance), namely 20, 40, 60, 80, 100, and 120 mm. The process parameters used are presented in Table 3.

**Table 3.** Process parameters.

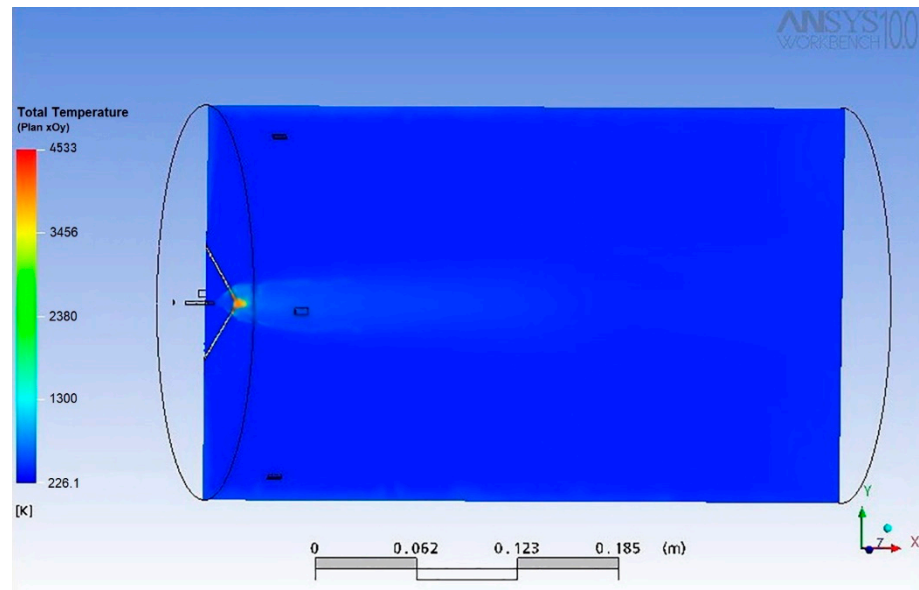
Parameters	Value
Current intensity (A)	140
Tension (voltage)	32
Pressure of compressed air (bar)	5
Movement speed of the gun (m/s)	0.11
Standoff distance (mm)	20/40/60/80/100/120

The morphology of the arc-sprayed coatings was observed by microstructural investigations carried out on the cross-section of the samples, using the scanning electronic microscope (SEM) Vega II LSH type (manufactured by Tescan, Brno, The Czech Republic).

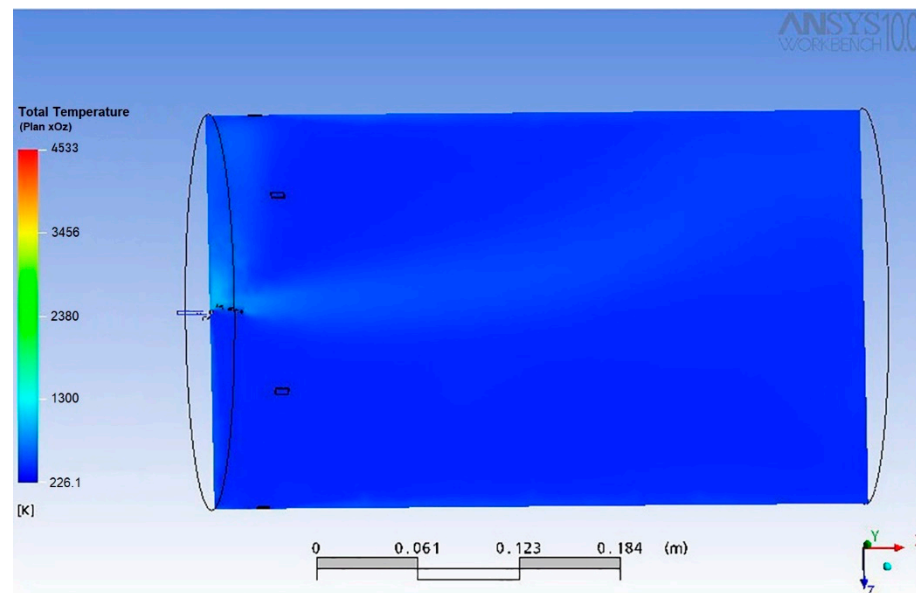
## 4. Results

### 4.1. Temperature Distribution in the Entrainment Gas Jet

The axial variation of the fluid temperature in the axial planes  $xOy$  and  $xOz$  is presented in Figure 4.



(a)



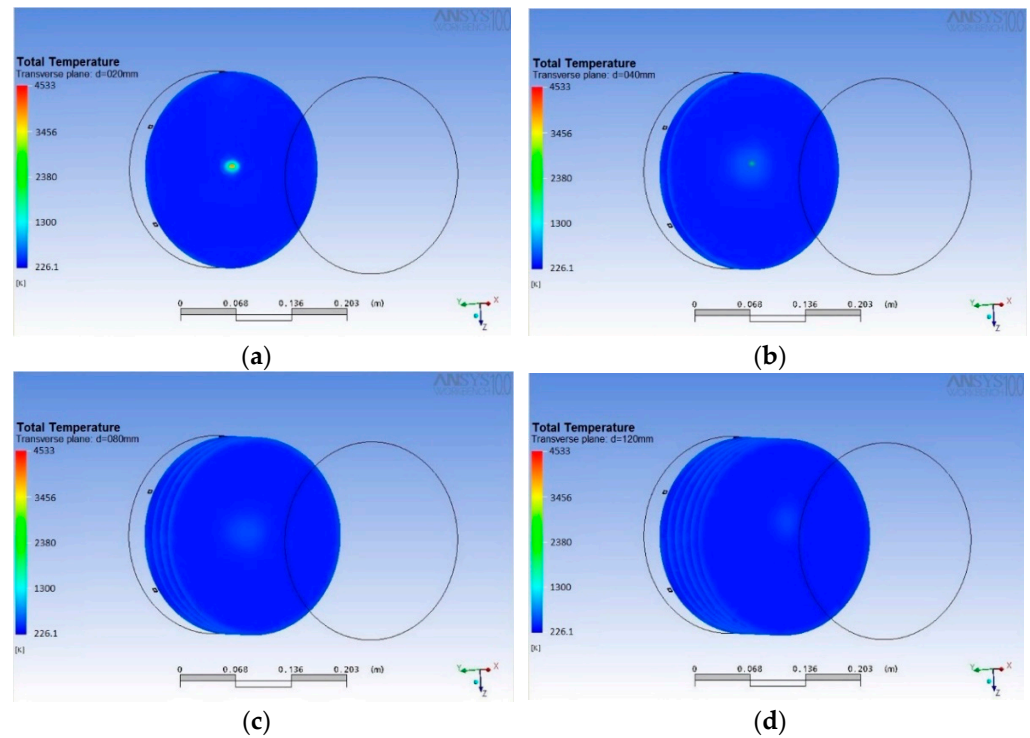
(b)

**Figure 4.** Fluid temperature variation: (a)  $xOy$  plan; (b)  $xOz$  plan.

The variation of the total fluid temperature in the family of planes perpendicular to the  $Ox$  axis is presented in Figure 5.

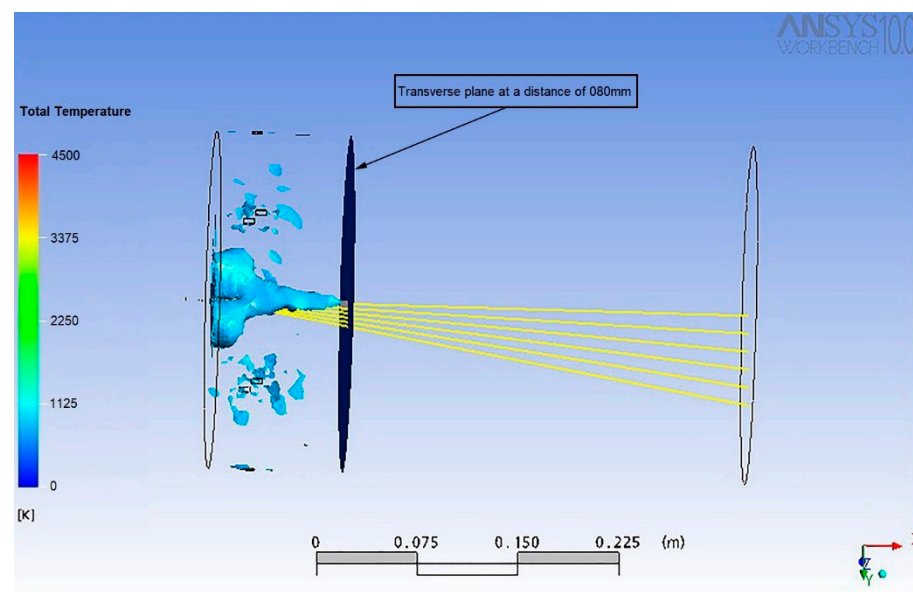
In the planes that are perpendicular to the axis of symmetry, as shown in Figure 5, it was observed that the jet temperature varies only in the central area of the plane up to the

one located at a distance of 80 mm from the contact point between the two wires, where the arc is formed (Figure 5c). In agreement with these, Figure 6 highlights that a temperature of the gaseous medium higher than 650 K, which could positively influence the temperature of the sprayed particles, according to Zare, M.A., et al. [49], can be encountered up to a distance of 80 mm from the spray nozzle.



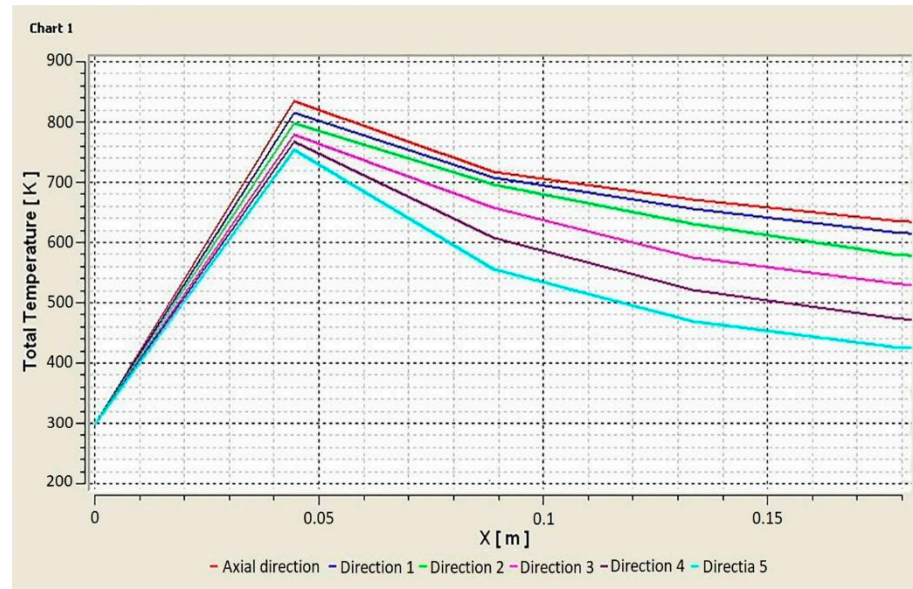
**Figure 5.** The distribution of the compressed air temperature, in perpendicular planes, located at distances of: (a) 20 mm; (b) 40 mm; (c) 80 mm; (d) 120 mm—from the wires' intersection point.

Figure 6 presents the 3D model of the isosurface, which has a constant temperature of 650 K and is generated during the arc spray process, inside the spray jet.

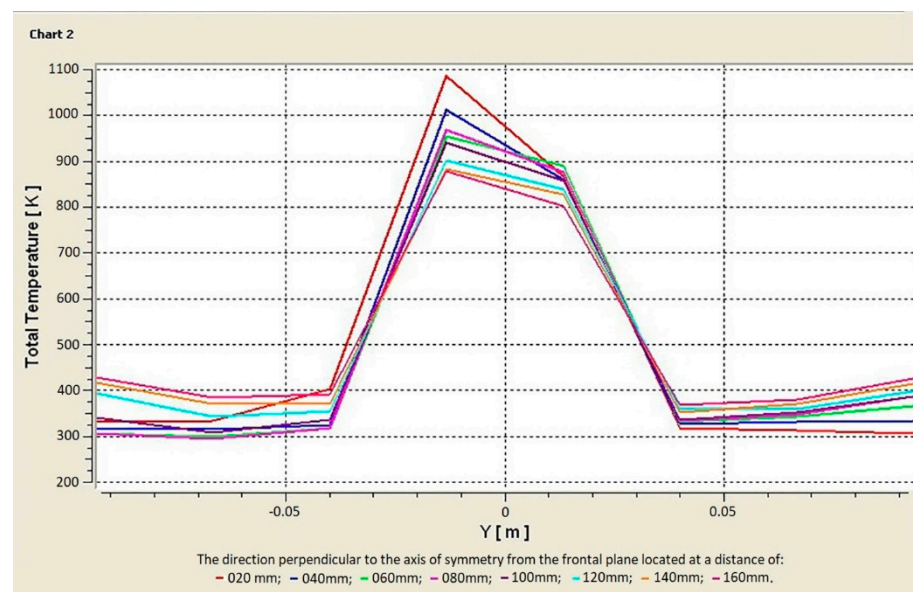


**Figure 6.** Three-dimensional model of the isosurface (at a constant temperature of 650 K).

The variation graphs of the fluid (compressed air) temperature are presented in Figure 7a,b, obtained according to inclined or perpendicular directions to the axis of symmetry of the model.



(a)



(b)

**Figure 7.** Fluid temperature variation inside the model: (a) in inclined directions with respect to the axis of symmetry; (b) in directions perpendicular to the axis of symmetry.

The analysis of the thermal field distribution within the model showed that in the classical thermal arc spraying process, due to the interaction between the gas jet and the electric arc, the gas temperature varies between the limits: 950 K and 300 K. The temperature of the gas jet varies differently in directions inclined to the axis of symmetry, as presented in Figure 7a. Thus, the fluid temperature variation curves inside the model, in directions inclined to the symmetry axis (Figure 7a), show maximum values of 850 K, around a distance of 40–50 mm from the nozzle, after which it decreases exponentially to the value of 300 K. The same aspect is observed in Figure 7b where the fluid temperature

reaches a maximum around 900 K, at a distance of 20 mm from the central axis in any plane perpendicular to the symmetry axis of the model, after which it drops dramatically to 300 K. It can be suggested that inside the model, in the first 20 mm from the point of contact between the wires, the compressed air heats up from the electric arc, through the phenomenon of forced convection, reaches a maximum temperature around 850–900 K, and then, decreases exponentially. The results shown in Figures 5–7 demonstrate that inside the model, in its axial region, a conical zone is formed where the fluid temperature is maximum. This zone, which we can suggestively call the spray jet, characterized by a high temperature (>650 K) and fluid flow velocity, influences the temperature and velocity of the sprayed particles.

#### 4.2. Numerical Results

A particle detached from the melt formed in the electric arc and propelled to the surface of the substrate by the entrainment gas jet will continuously cool, according to the thermal equilibrium Equation (4).

Equations (10) and (15) allow the determination of the instantaneous temperature of the particle during undercooling, based on Equation (17):

$$T_p = T_s - \frac{1}{k_i} \left( \frac{1}{3} D_1 \cdot x^3 + \frac{1}{2} D_2 \cdot x^2 + D_3 \cdot x + D_4 \cdot t \right) \quad (17)$$

To solve Equation (14), the numerical solution method (second-order Runge–Kutta method) was adopted, based on which the values of “ $x$ ” for the incrementing time “ $\partial t$ ” were obtained. These values of the incrementing time “ $x$ ” were introduced in Equation (17), and thus, the values of the particle temperature ( $T_p$ ) were determined.

Equation (17) does not take into account the phenomenon of diffusion in the solid state, characteristic between the components of an alloy, nor the one developed at the solid–liquid interface.

The diffusion frequency of the latent solidification heat decreases progressively and, at a specific moment, becomes equal to the frequency of heat dissipation in the gaseous medium. At this moment, the undercooling phenomenon ceases and the specific temperature is obtained imposing the condition  $\frac{\partial T}{\partial t} = 0$ . After that, the further solidification of the melt is carried out through the segregated solidification mechanism. At this stage, the solid fraction can be calculated using the Scheill equation, modified by Flemings [53,54] (18):

$$f_s = 1 - (1 - f_r \left\{ \frac{T_m - T_r}{T_m - T_p} \right\})^{\frac{1}{1-k_0}}, \quad (18)$$

The thermal profile of some aluminum particles is presented in Figure 8, for the particular case of the particle dimensions between 0.05 and 0.4 mm, obtained using Equation (17), considering a time interval of 0.025 s. The temperature of the fluid  $T_{fi}$  is variable, and its  $T_{fi}$  values correspond to Direction 3, represented in Figure 3b.

$C_{ps}$  was calculated with the relation;

$$C_p = a + b \cdot T_t + c \cdot T_t^2 \quad (19)$$

where  $a = 29.3$ ;  $b = 0$ ;  $c = 0$  for the liquid medium and  $a = 20.7$ ;  $b = 12.3 \times 10^3$ ;  $c = 0$  for the solid state [39].

The temperature variation graphic of the sprayed particle in the electric arc process, named the *thermal profile* (Figure 8), highlights that, initially, under the gas jet action, the particles' temperature decreases suddenly till the solidification temperature is reached, after which, it increases to the melting temperature and is followed by a new decreasing trend.

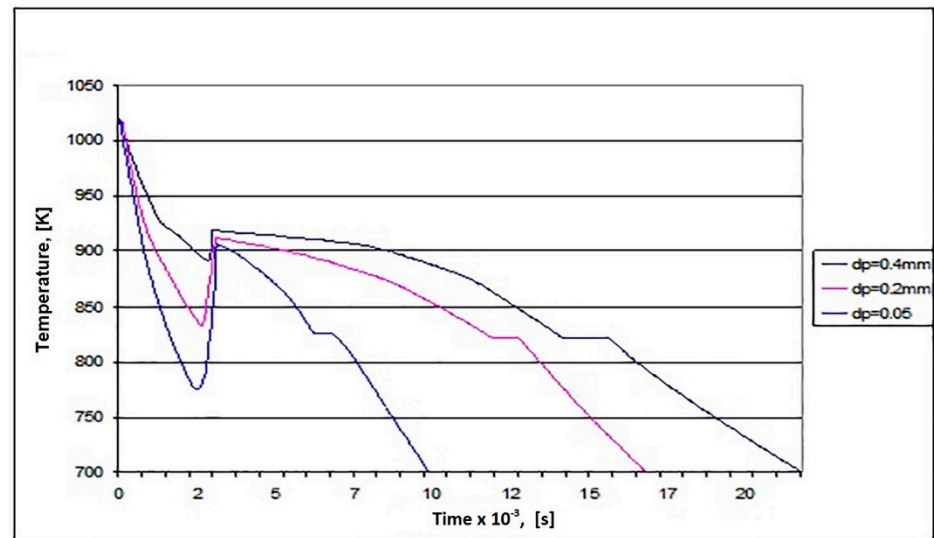


**Figure 8.** The temperature variation of some aluminum alloy particles (99.8% Al), with various dimensions, in the spray jet.

Table 4 presents the numerical constants that were used to calculate the temperature of the aluminum particles.

**Table 4.** Initial parameters.

Parameters	Symbol	Value
Latent melting heat of aluminum	$\lambda_p$	10.4 kJ/mol
Kinematic viscosity of compressed air	$\nu$	233.7 m <sup>2</sup> /s
Aluminum density	$\rho_p$	2700 Kg/m <sup>3</sup>
Compressed air density	$\rho_f$	1185 Kg/m <sup>3</sup>
Thermal conductivity of compressed air	$k_f$	0.58 cal·104/(grd·cm·s)
Specific heat of compressed air	$C_{pf}$	1192 J/(Kg·K)
Specific heat of liquid (aluminum)	$C_{pp}$	29.3 J/(K·mol)
Specific heat of solid (aluminum)	$C_{ps}$	11070 kJ/(K·mol)
Melting temperature of aluminum	$T_t$	933 K
Liquid phase temperature (aluminum)	$T_l$	1020 K

The sudden increase of the particles' temperature, in the time range of (0.02–0.04), is due to the latent heat released by the solidified fraction. The effect produced by the latent solidification heat is noticeable till the moment when its value becomes equal to the value of the energy dissipated by the particle to the gaseous medium.

The influencing factors of the thermal profile of the sprayed particles (highlighted by Equations (10) and (17)) are: particle dimension, the temperature of the gas jet, the velocity of the gas jet, the particle's velocity, and the nature of the wire's material.

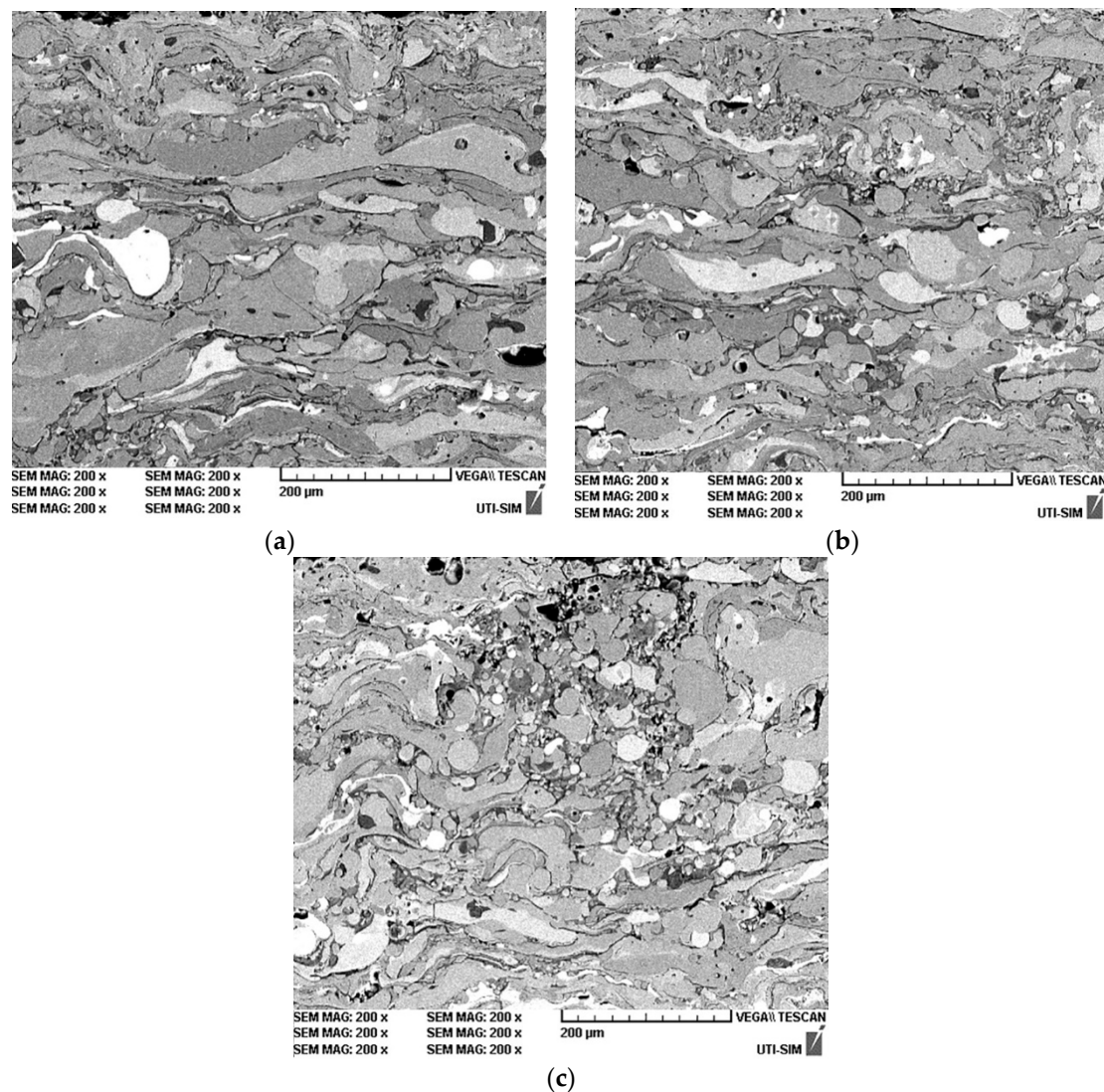
#### 4.3. Morphology Analysis of Experimental Coatings

Figure 9 shows secondary electron (SE) images on the cross-sections of 01S coatings obtained by electric arc thermal spraying at different spraying distances.

Aluminum alloy layers, obtained at distances under 40 mm, exfoliated from the substrate surface (were "burned") because of the intense thermal field generated by the electric arc. For these reasons, they were excluded from our following investigations.

Coatings obtained at distances  $d = 80$  mm showed a specific structure for the layers obtained by electric arc thermal spraying, consisting of: flattened particles, pores, and communicating channels between pores and oxides, as presented in Figure 9a. The small

average thickness of the splats and their uniform flattening suggest that the aluminum alloy particles were in a molten state at the time of impact.



**Figure 9.** SE images on the cross-section of the 01S coatings obtained by electric arc thermal spray, at spraying distances of: (a) 80 mm; (b) 100 mm; (c) 120 mm—from the wires' intersection point.

Aluminum alloy layers obtained at spray distances greater than 80 mm, presented in Figure 9b,c, contain pores, as well as unmelted particles embedded in a metallic matrix of flattened particles. The high average thickness of the flattened lamellae (splats), as well as the presence of non-fused particles in the layer suggest that, at the time of impact, the particles were in a semi-molten or even solid state. It can be observed that the number of unmelted particles in the layer increases with the increasing of the distance between the nozzle and the layer, as observed by comparing Figures Figure 9b,c. This observation strengthens our belief that the aluminum alloy particles cool intensely with increasing of the spray distance, which is in agreement with the analytical results previously presented.

## 5. Conclusions

In the case of the classical arc spraying process, one of the first observations that emerged from the analysis of the temperature field distribution inside the model was that the temperature of the gas jet varies between 950 and 300 K, as a result of the interaction between the electric arc formed between the two wires and the jet of gas.

Following the application of the equations, it was observed that the gas jet temperature variation occurs only in the central area of the planes perpendicular to the symmetry axis, up to a distance of 80 mm from the point of electric arc formation. This conclusion was validated by the morphology aspects observed on the cross-section of the experimental samples, which presented a specific lamellar structure at an 80 mm distance, respectively unmelted inclusions in the metallic matrix, more numerous with increasing of the spray distance.

The temperature variation of the particles sprayed during the arc deposition (it had a less usual path, since it decreased sharply until reaching the solidification temperature) was followed by an increase to a value close to the melting temperature and a new, much slower decrease. The nature of this variation profile (thermal profile) can be explained by the fact that we are dealing with a forced cooling phenomenon, which determines the fast cooling of the particle until the appearance of the solidification, followed by a rapid increase due to the latent heat of solidification ( $\lambda$ ).

The temperature rise effect due to the latent solidification heat was visible until its value was equalized by the heat transferred from the particle to the fluid (carrier gas). The time elapsed until the two values were equalized was directly proportional to the particle diameter and the difference between the particle temperature and the fluid temperature. Thus, it can be concluded that the main factors influencing the thermal profile of the particles sprayed by this process (electric arc) are the temperature of the fluid (of the gaseous medium), the nature of the wire material, and the size of the sprayed particles.

Knowing the temperature variation of the sprayed particles allows establishing their aggregation state, respectively determining the standoff distance, according to the characteristics of the material (melting temperature and solidification temperature), thus becoming a useful tool in optimizing the process parameters.

**Author Contributions:** Conceptualization, formal analysis—D.-L.C.; methodology, validation interpretation—S.L.T., software, writing—original draft preparation—A.-M.C. All authors have read and agreed to the published version of the manuscript.

**Funding:** This research received no external funding.

**Institutional Review Board Statement:** Not applicable.

**Informed Consent Statement:** Not applicable.

**Data Availability Statement:** Not applicable.

**Conflicts of Interest:** The authors declare no conflict of interest.

## Nomenclature

$f_s$	the percentual quantity of solidified fluid in the particle volume (%)
$\frac{\partial T}{\partial t}$	temperature variation of the particle in the time frame $\partial t$ (K/s)
$\frac{dx}{dt}$	Liquid–solid interface forward speed (m/s)
$\frac{\partial f_s}{\partial x}$	distance solidified fraction $\partial x$ (Kg/m)
$A_p$	particle surface area (m <sup>2</sup> )
$C_l$	specific heat of the liquid phase (J·Kg <sup>-1</sup> ·K <sup>-1</sup> )
$C_{pf}$	specific heat of the fluid (J/(Kg·K))
$C_{pp}$	specific heat at constant pressure of the liquid particle (J·Kg <sup>-1</sup> ·K <sup>-1</sup> )
$C_s$	specific heat of the solid phase (J·Kg <sup>-1</sup> ·K <sup>-1</sup> )
$d_p$	particle diameter (m)
$f_r$	the fraction of liquid solidified during cooling (Kg)
$h$	thermodynamic enthalpy (J)
$h_{tot}$	total specific enthalpy of the fluid (J)
$k_0$	partition coefficient, $k_0 = 0.14$
$k_g$	thermal conductivity of the gas (W/(m·K))
$k_i$	coefficient attached to the interface (m·s <sup>-1</sup> ·T <sup>-1</sup> )

p	thermodynamic pressure (Pa)
Pr	Prandtl number
Re	Reynolds number
$S_E$	internal source of energy, $S_E = 0$ (J)
$S_M$	internal moment, $S_M = 0$ (J)
t	time (s)
T	temperature of the fluid on components: $T_x, T_y, T_z$ (K)
$T_f$	drive gas temperature, (K)
$T_L$	liquid temperature—specific to each alloy (K)
$T_m$	melting temperature of the element with the lowest melting point in the alloy composition (K)
$T_p$	particle's temperature i (K)
$T_r$	cessation temperature of the subcooling (K)
$T_s$	the solidification temperature specific to each material (K),
$v_f$	fluid velocity with the components: $v_{fx}, v_{fy}, v_{fz}$ (m/s)
$v_g$	fluid velocity (m/s)
$V_p$	particle's volume ( $m^3$ )
$v_p$	particle velocity (m/s)
x	the length of displacement by the solidification front ( $J \cdot Kg^{-1} \cdot K^{-1}$ )
<i>Greek letters</i>	
$\alpha_f$	convection heat exchange coefficient ( $W \cdot m^{-2} K^{-1}$ )
$\delta$	identical matrix
$\eta$	dynamic viscosity (Pa·s)
$\lambda$	thermal conductivity (W/mK)
$\nu$	kinematic viscosity ( $N \cdot s/m^2$ )
$\rho$	density of the compressed air ( $Kg/m^3$ )
$\eta_f$	dynamic viscosity of the fluid (Pa·s)
$\lambda_p$	latent solidification heat (released by the solidified liquid fraction $f_s \cdot V_p$ ) (J/Kg)
$\lambda_u$	latent heat of solidification of the table unit (J/Kg)
$\rho_f$	fluid density ( $Kg/m^3$ )
$\rho_p$	molten particle density ( $Kg/m^3$ )

## References

1. Pawłowski, L. *The Science and Engineering of Thermal Spray Coatings*, 2nd ed.; John Wiley & Sons Ltd.: England, UK, 2008; ISBN 978-0-471-49049-4.
2. Bejinariu, C.; Burduhos-Nergis, D.P.; Cimpoesu, N.; Bernevig-Sava, A.; Toma, S.L. Study on the anticorrosive phosphated steel carabiners used at personal protective equipment. *Qual. Access Success* **2019**, *20*, 71–76.
3. Toma, B.F.; Baci, R.E.; Bejinariu, C.; Cimpoiesu, N.; Ciuntu, B.M.; Toma, S.L.; Burduhos-Nergis, D.P.; Timofte, D. Researches on the improvement of the bioactivity of  $TiO_2$  deposits, obtained by magnetron sputtering–DC. *IOP Conf. Ser. Mat. Sci. Eng.* **2018**, *374*, 012017. [\[CrossRef\]](#)
4. Toma, S.L.; Bejinariu, C.; Baci, R.; Radu, S. The effect of frontal nozzle geometry and gas pressure on the steel coating properties obtained by wire arc spraying. *Surf. Coat. Technol.* **2013**, *220*, 266–270. [\[CrossRef\]](#)
5. Paulin, C.; Chicet, D.; Paleu, V.; Benchea, M.; Lupescu, M.; Munteanu, C. Dry friction aspects of Ni-based self-fluxing flame sprayed coatings. *IOP Conf. Ser. Mater. Sci. Eng.* **2017**, *227*, 012091. [\[CrossRef\]](#)
6. Panturu, M.; Chicet, D.; Lupescu, S.; Istrate, B.; Munteanu, C. Applications of ceramic coatings as TBCs on the internal combustion engine valves. *Acta Tech. Napoc. Ser. Appl. Math. Mech. Eng.* **2018**, *61*, 137–142.
7. Newbery, A.P.; Grant, P.S. Droplet Splashing during Arc Spraying of Steel and the Effect on Deposit Microstructure. *J. Therm. Spray Technol.* **2000**, *9*, 250–258. [\[CrossRef\]](#)
8. Steffens, H.D.; Nassenstein, K. Influence of the Spray Velocity on Arc-Sprayed Coating Structures. *J. Therm. Spray Technol.* **1999**, *8*, 454–460. [\[CrossRef\]](#)
9. Stescu, C.; Chicet, D.; Tufescu, A.; Istrate, B.; Munteanu, C.; Strugaru-Iacob, S. Contact stress simulation problem in case of thermal spray coatings. *IOP Conf. Ser. Mater. Sci. Eng.* **2020**, *916*, 012114. [\[CrossRef\]](#)
10. Chicet, D.; Tufescu, A.; Paulin, C.; Panțuru, M.; Munteanu, C. The Simulation of Point Contact Stress State for APS Coatings. *IOP Conf. Ser. Mater. Sci. Eng.* **2017**, *209*, 12044. [\[CrossRef\]](#)
11. Toma, S.L.; Haraga, R.A.; Chicet, D.L.; Paleu, V.; Bejinariu, C. Hard Alloys with High Content of WC and TiC—Deposited by Arc Spraying Process. In *Welding-Modern Topics*; Alfaro, S.C.A., Borek, W., Tomiczek, B., Eds.; IntechOpen: London, UK, 2020. [\[CrossRef\]](#)

12. Wang, X.; Heberlein, J.; Pfender, E.; Gerberich, W. Effect of Nozzle Configuration, Gas Pressure, and Gas Type on Coating Properties in Wire Arc Spray. *J. Therm. Spray Technol.* **1999**, *8*, 565–575. [[CrossRef](#)]
13. Gedzevicius, I.; Valiulis, A.V. Influence of the particles velocity on the arc spraying coating adhesion. *Mater. Sci.* **2003**, *9*, 334–337.
14. Gedzevicius, I.; Valiulis, A. Analysis of wire arc spraying process variables on coatings properties. *J. Mater. Process. Technol.* **2006**, *175*, 206–211. [[CrossRef](#)]
15. Watanabe, T.; Usui, M. Effect of Atomizing Gas on Oxidation of Droplets in Wire Arc Spraying. *J. Jpn. Inst. Met.* **1999**, *63*, 98–102. [[CrossRef](#)]
16. Kawase, R.; Kureishi, M.; Minehisa, S. Relation between arc spraying condition and adhesion strength of sprayed coatings (Report 1). *Transact. Jpn. Weld. Soc.* **1984**, *15*, 27–33.
17. Kant, S.; Kumar, M.; Chawla, V.; Singh, S. Study of High Temperature Oxidation Behavior of Wire Arc Sprayed Coatings. *Mater. Today Proc.* **2020**, *21*, 1741–1748. [[CrossRef](#)]
18. Schilder, B.; Garling, A.; Reimer, F.; Hamann, M.; Joos, R.; Hüger, J.; Pöhlmann, M.; Lampke, T. CFD Enhanced Thermal Spray Process for Coating of Cylinder Bores of Car Engines. *J. Therm. Spray Technol.* **2020**, *29*, 546–559. [[CrossRef](#)]
19. Kawase, R.; Kureishi, M.; Maehara, K. Arc phenomenon and wire fusion in arc-spraying (Report 2). *Transact. Jpn. Weld. Soc.* **1984**, *15*, 66.
20. Arbogast, J.; Schaller, R.; Lindemann, S.; Schilder, B.; Rohde, M.; Seifert, H.J. Thermal wave interferometry measurements and microstructural analysis of twin wire arc spray cylinder coatings for passenger car engines. *Infrared Phys. Technol.* **2020**, *105*, 103216. [[CrossRef](#)]
21. Toma, S.L. The influence of jet gas temperature on the characteristics of steel coating obtained by wire arc spraying. *Surf. Coat. Technol.* **2012**, *220*, 261–265. [[CrossRef](#)]
22. Toma, B.F.; Nanu, C.; Popescu, C.; Socolov, R.V.; Rosu, V.-E.; Toma, S.L.; Himiniuc, L.M.; Rosu, S.T. The Analysis with Finite Elements of the Elasto-plastic Behaviour of the Spinal Immobilizers-in the Case of Comminutive Fractures. *Mater. Plast.* **2019**, *57*, 253–264. [[CrossRef](#)]
23. Nanu, C.; Poeata, I.; Popescu, C.; Eva, L.; Toma, B.F.; Toma, S.L. The Influence of the Characteristics of Plastic Materials Used in the Performance of the Thoraco-Lumbar Orthoses. *Mater. Plast.* **2018**, *55*, 85–90. [[CrossRef](#)]
24. Calin, M.A.; Curteza, A.; Toma, S.; Agop, M. Morphological properties of polyamide 6-cnt nanofibers obtained by electrospinning method. *Metal. Int.* **2013**, *18*, 19–22.
25. Tamaki, R.; Yamakawa, M. Study on the nozzle jet in arc spraying. *Appl. Math. Mech.* **2016**, *37*, 1394–1402.
26. Tamaki, R.; Yamakawa, M. Elucidation of mechanism for reducing porosity in electric arc spraying through CFD. *Lect. Notes Comput. Sci.* **2018**, *10860*, 418–428. [[CrossRef](#)]
27. Tamaki, R.; Yamakawa, M. Effect of plate mounted between two wires in electric arc spraying. *J. Comput. Sci.* **2019**, *32*, 56–67. [[CrossRef](#)]
28. Chen, Y.; Liang, X.; Liu, Y.; Xu, B. Numerical analysis of the effect of arc spray gun configuration parameters on the external gas flow. *J. Mater. Process. Technol.* **2009**, *209*, 5924–5931. [[CrossRef](#)]
29. Liao, H.; Zhu, Y.; Bolot, R.; Coddet, C.; Ma, S. Size distribution of particles from individual wires and the effects of nozzle geometry in twin wire arc spraying. *Surf. Coat. Technol.* **2005**, *200*, 2123–2130. [[CrossRef](#)]
30. Bolot, R.; Planche, M.-P.; Liao, H.; Coddet, C. A three-dimensional model of the wire-arc spray process and its experimental validation. *J. Mater. Process. Technol.* **2008**, *200*, 94–105. [[CrossRef](#)]
31. Shukla, R.K.; Kumar, A.; Kumar, R.; Singh, D.; Kumar, A. Numerical study of pore formation in thermal spray coating process by investigating dynamics of air entrapment. *Surf. Coat. Technol.* **2019**, *378*, 124972. [[CrossRef](#)]
32. Leither, C.; Risan, J.; Bashirzadeh, M.; Azarmi, F. Determination of the elastic modulus of wire arc sprayed alloy 625 using experimental, analytical, and numerical simulations. *Surf. Coat. Technol.* **2013**, *235*, 611–619. [[CrossRef](#)]
33. Tian, H.; Wang, C.; Guo, M.; Tang, Z.; Tong, H.; Wang, X.; Wei, S.; Xu, B. A residual stresses numerical simulation and the relevant thermal-mechanical mapping relationship of Fe-based coatings. *Results Phys.* **2019**, *13*, 102195. [[CrossRef](#)]
34. Wen, K.; Liu, X.; Zhou, K.; Liu, M.; Zhu, H.; Huang, J.; Zhang, Z.; Huang, R.; Mao, J.; Yan, X.; et al. 3D time-dependent numerical simulation for atmospheric plasma spraying. *Surf. Coat. Technol.* **2018**, *371*, 344–354. [[CrossRef](#)]
35. Zhong, L.; Gu, Q.; Wu, B. Deep learning for thermal plasma simulation: Solving 1-D arc model as an example. *Comput. Phys. Commun.* **2020**, *257*, 107496. [[CrossRef](#)]
36. Zhang, H.-Y.; Liu, S.-H.; Li, C.-J.; Li, C.-X. Deposition and oxidation behavior of atmospheric laminar plasma sprayed Mo coatings from 200 mm to 400 mm under 20 kW: Numerical and experimental analyses. *Surf. Coat. Technol.* **2020**, *400*, 126245. [[CrossRef](#)]
37. Bhusal, S.; Zhang, C.; Bustillos, J.; Nautiyal, P.; Boesl, B.; Agarwal, A. A computational approach for predicting microstructure and mechanical properties of plasma sprayed ceramic coatings from powder to bulk. *Surf. Coat. Technol.* **2019**, *374*, 1–11. [[CrossRef](#)]
38. Ding, S.-Y.; He, P.-F.; Ma, G.-Z.; Wu, Z.-Y.; Tang, L.; Chen, S.-Y.; Xing, Z.-G.; Wang, H.-D.; Xu, B.-S. Investigation on the removal of suspended particles during internal rotating plasma spraying using numerical and experimental methods. *Surf. Coat. Technol.* **2020**, *393*, 125731. [[CrossRef](#)]
39. Bobzin, K.; Bagcivan, N.; Petkovic, I. Numerical and experimental determination of plasma temperature during air plasma spraying with a multiple cathodes torch. *J. Mater. Process. Technol.* **2011**, *211*, 1620–1628. [[CrossRef](#)]
40. Selvan, B.; Ramachandran, K.; Sreekumar, K.; Thiyagarajan, T.; Ananthapadmanabhan, P. Numerical and experimental studies on DC plasma spray torch. *Vacuum* **2009**, *84*, 444–452. [[CrossRef](#)]

41. Wen, K.; Liu, X.; Liu, M.; Zhou, K.; Long, H.; Deng, C.; Mao, J.; Yan, X.; Liao, H. Numerical simulation and experimental study of Ar-H<sub>2</sub> DC atmospheric plasma spraying. *Surf. Coat. Technol.* **2019**, *371*, 312–321. [[CrossRef](#)]
42. Zhang, D.; Zheng, L.; Hu, X.; Zhang, H. Numerical studies of arc plasma generation in single cathode and three-cathode plasma torch and its impact on plasma spraying. *Int. J. Heat Mass Transf.* **2016**, *98*, 508–522. [[CrossRef](#)]
43. Savinkin, V.V.; Vizureanu, P.; Sandu, A.V.; Ratushnaya, T.Y.; Ivanischev, A.A.; Surleva, A. Improvement of the Turbine Blade Surface Phase Structure Recovered by Plasma Spraying. *Coatings* **2020**, *10*, 62. [[CrossRef](#)]
44. Cazac, A.M.; Bejinariu, C.; Baciuc, C.; Toma, S.L.; Florea, C.D. Experimental Determination of Force and Deformation Stress in Nanostructuring Aluminum by Multiaxial Forging Method. *Appl. Mech. Mater.* **2014**, *657*, 137–141. [[CrossRef](#)]
45. Baltatu, I.; Sandu, A.V.; Baltatu, M.S.; Benchea, M.; Achitei, D.C.; Ciolacu, F.; Perju, M.C.; Vizureanu, P.; Benea, L. Structural and physical characterization of new ti-based alloys. *Arch. Metall. Mater.* **2022**, *67*, 255–259. [[CrossRef](#)]
46. David, J.R. (Ed.) *Handbook of Thermal Spray Technology*; Davis & Associates: Materials Park, OH, USA, 2004.
47. Vardelle, M.; Leger, A.C.; Fauchais, P.; Gobin, D. Influence of particle parameters at impact on splat formation and solidification in plasma spraying processes. *J. Therm. Spray Technol.* **1995**, *4*, 50–58. [[CrossRef](#)]
48. Li, Y.; Xia, W.; Qin, J.; Zhao, D.; Zuo, M. The special chemical short-range order and solidification behavior of Cu–Fe–P immiscible alloys. *J. Mol. Liq.* **2021**, *344*, 117936. [[CrossRef](#)]
49. Zare, M.A.; Taghiabadi, R.; Ghoncheh, M.H. Effect of Cooling Rate on Microstructure and Mechanical Properties of AA5056 Al-Mg Alloy. *Int. J. Met.* **2021**, 1–11. [[CrossRef](#)]
50. Jegede, O.E.; Haque, N.; Mullis, A.M.; Cochrane, R.F. Relationship between cooling rate and SDAS in liquid phase separated metastable Cu-Co alloys. *J. Alloy Compd.* **2021**, *883*, 160823. [[CrossRef](#)]
51. Osório, W.R.; Garcia, A. Modeling dendritic structure and mechanical properties of Zn–Al alloys as a function of solidification conditions. *Mater. Sci. Eng. A* **2002**, *325*, 103–111. [[CrossRef](#)]
52. Cantor, B. Microstructure development during rapid solidification. In *Proceedings of the 22nd Risø International Symposium on Materials Science: Science of Metastable and Nanocrystalline Alloys, Roskilde, Denmark, 3–7 September 2001*; Dinesen, A., Eldrup, M., Jensen, D., Linderoth, S., Penderson, T., Pryds, N., Pendersen, A., Wert, J., Eds.; Riso National Laboratory: Roskilde, Denmark; pp. 483–493.
53. Flemings, M.C. Solidification processing. *Met. Mater. Trans. A* **1974**, *5*, 2121–2134. [[CrossRef](#)]
54. Flemings, M.C. Our Understanding of Macrosegregation. Past and Present. *ISIJ Int.* **2000**, *40*, 833–841. [[CrossRef](#)]